



Benchmarking of manganese oxide materials with CO oxidation as catalysts for low temperature selective oxidation

Lakshitha Pahalagedara^a, David A. Kriz^a, Niluka Wasalathanthri^a, Chandima Weerakkody^a, Yongtao Meng^a, Shanka Dissanayake^a, Madhavi Pahalagedara^a, Zhu Luo^b, Steven L. Suib^{a,b,c,*}, Partha Nandi^{d,**}, Randall J. Meyer^d

^a Unit 3060, Department of Chemistry, University of Connecticut, Storrs, CT 06269-3060, United States

^b Institute of Materials Science, University of Connecticut, Storrs, CT 06269, United States

^c Department of Chemical and Biomolecular Engineering, University of Connecticut, Storrs, CT 06269, United States

^d Corporate Strategic Research, ExxonMobil Research and Engineering, Annondale, NJ 08801

ARTICLE INFO

Article history:

Received 28 June 2016

Received in revised form 5 November 2016

Accepted 21 November 2016

Available online 22 November 2016

Keywords:

Carbon monoxide oxidation

Octahedral molecular sieve catalysts

Transition metal ion doped manganese

oxide

ABSTRACT

CO oxidation behavior of different manganese oxide materials was studied as a model probe reaction to benchmark catalytic activities that could be useful for other aerobic oxidations. K-OMS-2, which showed intermediate activity [$E_a = 3.0$ and 6.3 kcal/mol for K-OMS-2 (made in solvent free procedure or SF) and K-OMS-2 (made via hydrothermal route or REF) respectively], were chosen for metal dopant studies using microwave assisted hydrothermal synthesis. These were further characterized using X-ray diffraction (XRD), N_2 sorption, Raman spectroscopy, scanning electron microscopy (SEM), and carbon monoxide temperature programmed reduction (CO-TPR). Additional characterization was carried out for Ni-K-OMS-2 materials using atomic absorption spectroscopy (AAS) and thermogravimetric analysis-mass spectroscopy (TGA-MS). Doping K-OMS-2 with Ni resulted in a large increase in oxygen mobility and re-adsorption, and the moderate activation energy for CO oxidation (13 kcal/mol) by Ni-K-OMS-2(SF) suggests that Ni-doped materials are good candidates for low temperature selective oxidation.

© 2016 Elsevier B.V. All rights reserved.

1. Introduction

Carbon monoxide is generated by various human activities and causes many adverse effects on humans and the environment [1–3]. CO is a tasteless, odorless, and colorless poisonous gas and is directly involved in the formation of ground-level ozone. As a result, the presence of CO influences atmospheric chemistry and hence the climate [3]. Therefore, carbon monoxide oxidation catalysis has become an important research area in the fields of chemical sensors, purification devices, automobile emissions, and proton exchange membrane fuel cells. The amount of carbon monoxide in urban areas has reached much higher levels due to an increased number of automobiles. CO oxidation studies also involve controlling CO generated by incomplete combustion processes. The incomplete combustion of fuels, including hydrocarbons, gas, wood

and charcoal, leads to CO emission as an intermediate reaction product [4]. Hence, CO oxidation can be used as a probe in order to study the low temperature partial oxidation of hydrocarbons.

CO oxidation catalysis has been widely studied using noble metal catalysts such as Pt, Ru, and Au supported on reducible metal oxides. Since these noble metal catalysts are expensive, studies have been carried out using relatively cheap transition metal alternatives such as metal oxides, spinels, perovskites, hopcalite, and alloys. Hopcalite is the most widely used commercial catalyst for respiratory protection; however, this material shows low activity at ambient temperature and is readily deactivated in the presence of moisture. Similarly, the low temperature activation of C–H bonds is mostly reported based on Hg, Pd, Pt, and Au [1,5,6]. Chen et al. developed a manganese oxide based catalyst for the low temperature methane partial oxidation [7]. The high activity is attributed to the interconversion of Mn(II), Mn(III), and Mn(IV) under methane oxidation conditions. However, this work was performed in the presence of trifluoroacetic acid. Therefore, the development of a low temperature, environmentally benign catalyst with low cost, high activity, increased selectivity, and ability to function under different environments for prolonged time

* Corresponding author at: Unit 3060, Department of Chemistry, University of Connecticut, Storrs, CT 06269-3060, United States.

** Corresponding author.

E-mail addresses: Steven.Suib@uconn.edu (S.L. Suib), Partha.Nandi@ExxonMobil.com (P. Nandi).

periods remains a significant challenge. Manganese is one of the most naturally abundant elements, has low toxicity, and manganese compounds have captured the attention of researchers as an attractive catalyst for an array of oxidation reactions. Moreover, manganese oxides are more complicated than many other oxides, having more than twenty polymorphs, and the catalytic activities of manganese oxides depend on their chemical compositions, crystallographic structures, morphologies, and pore structures. Manganese oxide octahedral molecular sieves (OMS) are microporous inorganic nanostructures and they possess catalytic activities and semiconducting properties due to their mixed valent lattice structures consisting of Mn^{2+} , Mn^{3+} and Mn^{4+} [7]. The most extensively studied OMS material is cryptomelane (OMS-2), which has a one-dimensional tunnel structure composed of edge-shared MnO_6 octahedra that form a 2×2 arrangement (2 represents the number of linked octahedral per tunnel side) of $0.46 \text{ nm} \times 0.46 \text{ nm}$ size. In OMS-2, Mn^{2+} , Mn^{3+} and Mn^{4+} reside in the framework sites and K^+ resides in the tunnel sites. The average oxidation state of the Mn is $+3.8$ and K^+ compensates the charge imbalance due to the reduction of Mn^{4+} [8]. By comparison to many other mixed metal oxides, OMS-2 materials are hydrophobic and therefore have improved hydrolytic stability under oxidation reaction conditions [9,10]. The preparation method of OMS-2 influences its catalytic activity by modifying surface area, average oxidation state, particle size, morphology, crystallinity, stability, and other properties. Moreover, by incorporating metal ions into the tunnels or the framework sites these properties and the catalytic activity of the OMS-2 materials can be tuned [8].

In another study, Ozacar et al. explored the effects of silver doping in cryptomelane and silver hollandite (Ag-OMS-2) OMS materials on CO oxidation reactions [1]. The materials were synthesized by microwave reflux and hydrothermal methods and CO oxidation was proposed to follow the Mars-van Krevelen mechanism, where lattice oxygen atoms of manganese oxides are the active species for CO oxidation and the consumed lattice oxygen sites are restored by gaseous oxygen. Genuino et al. incorporated V^{5+} into the framework of OMS-2 and varied the V:Mn elemental ratios using a simple reflux synthesis method [11]. The activity of the catalyst increased with an increase of O_2 concentration in the feed gas and the V-incorporated catalyst was more resistant to water poisoning than the undoped K-OMS-2. According to previous studies on catalytic oxidation using metal ion doped K-OMS-2 materials, dopant metal ions such as Cs^+ and Ag^+ are mostly used for total oxidation [1,12] whereas metal ions such as Na^+ , Co^{2+} , Ni^{2+} , Cr^{3+} , Zn^{2+} , W^{6+} , Mo^{6+} , Al^{3+} , and Fe^{3+} are widely used for selective oxidation [11,13,14]. On the other hand, Cu^{2+} , V^{5+} , and Ce^{4+} doped K-OMS-2 materials are used as catalysts for both total and selective oxidation [11,15–17].

There are a multitude of different types of active sites in these materials due to varying size of crystallite sizes, varying amounts of oxygen vacancies, defects and strains, amount and distribution of the dopants in these materials. In the current manuscript, we are not trying to deconvolute the complexities arising from these factors discussed above. Instead, we are to use the experimentally determined apparent activation energies in these materials for catalyst benchmarking.

In this study, we report the synthesis of Na-OMS-2, K-OMS-2(REF), K-OMS-2(SF), Cs-OMS-2, and metal ion doped K-OMS-2 (M-K-OMS-2, where M represents a transition metal dopant) [7]. Among the M-K-OMS-2 materials, Ni and Rh-doped K-OMS-2 materials were extensively studied. They were synthesized using different synthesis methods and thoroughly characterized in order to elucidate the factors affecting their CO oxidation activity by establishing potential relationships between physicochemical properties and catalytic activities. The redox properties of these materials were investigated by CO temperature programmed

reduction (TPR) analysis and the depletion of structural oxygen and CO_2 evolution was studied using thermogravimetric analysis-mass spectrometry (TGA-MS) methods. Activity-versus-time curves were obtained in order to investigate catalyst deactivation. Moreover, these studies were used to understand the effects due to transition metal doping on the mobility of oxygen species and reducibility of Mn^{4+} ions in K-OMS-2 and how they play an important role in catalyzing CO oxidation [18,19]. Finally, the activities of these materials at temperatures giving 10% CO conversion (T_{10}) were summarized as a function of the surface area and amount of Ni and Rh. The obtained summary plot leads to an identification of materials which allows for a comparison between the materials that is useful when selecting a catalyst for other oxidation reactions. In addition, the calculated activation energy data for CO oxidation by different metal ion doped K-OMS-2 materials were used as a probe to identify the nature of the reactions that they catalyze; whether that is selective oxidation or total oxidation or both.

2. Experimental methods

2.1. Synthesis of manganese oxide materials

2.1.1. Na-OMS-2 (tunnel 2×2 , cryptomelane)

The synthesis was done by dissolving 1.7 g of $\text{NaMnO}_4 \cdot \text{H}_2\text{O}$ and 0.68 g of $\text{MnSO}_4 \cdot \text{H}_2\text{O}$ in 60 mL of distilled deionized water (DDW). The well dissolved mixture was transferred to a Teflon-lined autoclave and placed in an oven maintained at 240°C for 4 days. After cooling, the resulting products were isolated and washed with DDW five times using a centrifuge, and then dried at 80°C overnight.

2.1.2. Cs-OMS-2 (tunnel 2×2 , cryptomelane)

K-OMS-2 was added to an aqueous solution containing CsNO_3 and kept at 90°C for 3 h. The Cs^+ exchanged material was then washed and dried at 120°C overnight.

2.1.3. K-OMS-2(REF)/M-K-OMS-2(REF)

To a 500 mL round-bottomed flask containing potassium permanganate solution (0.40 mol/L, 225 mL) fitted with a condenser, a mixture of manganese sulfate solution (1.75 mol/L, 67.5 mL) and concentrated nitric acid (6.8 mL) was added. The dark brown slurry was refluxed for 24 h, then filtered and washed with deionized water several times. The catalyst was dried at 120°C overnight before use. Ni and Rh-doped K-OMS-2 were synthesized by adding 10 mmol of $\text{Ni}(\text{NO}_3)_2 \cdot 6\text{H}_2\text{O}$ and 2 mmol RhI_3 in the manganese sulfate solution, which results in a nominal Ni/Mn ratio of 1:20 and Rh/Mn ratio of 1:100. The final samples are denoted as Ni-K-OMS-2(REF) and Rh-K-OMS-2(REF) respectively. Metal ion doped K-OMS-2 (M-K-OMS-2) materials were synthesized by a similar reflux procedure by adding metal dopant precursor in the manganese salt mixture. The final sample is denoted as M-K-OMS-2(REF). The details of the preparation of other M-K-OMS-2 materials are provided in the literature [20,21].

2.1.4. K-OMS-2(SF)/M-K-OMS-2(SF)

9 mmol of $\text{Mn}(\text{Ac})_2 \cdot 4\text{H}_2\text{O}$ was mixed together with 6 mmol of KMnO_4 ($\text{Mn}^{2+}:\text{Mn}^{7+} = 3:2$) in an agate mortar and ground for 20 min. The dark purple colored powder mixture was then transferred to a glass vial, capped, and kept at 80°C for 4 h. The resulting fine black powder was cooled and washed with distilled deionized water (DDW) five times and then dried at 80°C overnight. Ni and Rh-doped K-OMS-2 were synthesized by adding 0.75 mmol of $\text{Ni}(\text{NO}_3)_2 \cdot 6\text{H}_2\text{O}$ and 0.15 mmol RhI_3 in the manganese salt mixture, which results in a nominal Ni/Mn ratio of 1:20 and Rh/Mn ratio of 1:100. The final samples are denoted as Ni-K-OMS(SF) and Rh-K-OMS(SF) respectively. M-K-OMS-2 materials were synthesized by a

similar solvent free procedure by adding a metal dopant precursor to the manganese salt mixture. The final samples are denoted as M-K-OMS-2(SF).

2.1.5. K-OMS-2(MWHY)/M-K-OMS-2(MWHY)

K_2SO_4 (0.2387 mol/L), $K_2S_2O_8$ (0.2387 mol/L), and $MnSO_4 \cdot H_2O$ (0.159 mol/L) were dissolved in 10.0 mL of distilled, deionized water (DDW). The aqueous reaction mixture was prepared in a 20 mL quartz reaction vial equipped with a magnetic stirrer, and then sealed with a cap. The synthesis was carried out in a Biotage Initiator microwave synthesizer programmed to heat up to 160 °C with a hold time of 10 min. Ni and Rh doped K-OMS-2 were synthesized by a similar MWHY procedure by adding 0.08 mmol of $Ni(NO_3)_2 \cdot 6H_2O$ and 0.02 mmol of RhI_3 in the manganese salt mixture, which results in a nominal Ni/Mn ratio of 1:20 and Rh/Mn ratio of 1:100. The final samples are denoted as Ni-K-OMS-2(MWHY) and Rh-K-OMS-2(MWHY) respectively.

2.2. Characterization of manganese oxide materials

2.2.1. X-ray diffraction (XRD) studies

XRD studies were performed with a Rigaku Ultima IV diffractometer using Cu $K\alpha$ ($\lambda = 0.15406$ nm) radiation. Crystal phases were identified using the International Center for Diffraction Data (ICDD) database.

2.2.2. Nitrogen sorption studies

The nitrogen sorption experiments were done using a Quantachrome Autosorb iQ₂ surface area system. All samples were degassed at 150 °C for 6 h prior to the nitrogen sorption experiment.

2.2.3. Field emission scanning electron microscopy (FESEM)

The FESEM imaging of the metal oxides was studied by using a FEI Nova NanoSEM 450 FESEM with a Schottky emitter operating at 2.0 kV.

2.2.4. Raman spectroscopy

A Reinshaw 2000 Ramascope attached to a CCD camera coupled with an Ar⁺ laser (514.4 nm) as the excitation source were used for the Raman experiments.

2.2.5. Inductively coupled plasma optical emission spectrometer (ICP-OES)

A PerkinElmer Optima 7300DV inductively coupled plasma optical emission spectrometer (ICP-OES) was used to determine the amounts of Ni and Rh.

2.2.6. Thermogravimetric mass spectrometry (TGA-MS)

TGA-MS was completed using a Netzsch Libra TG209 F1 thermogravimetric analyzer coupled to a Netzsch Aëolos QMS 403C quadrupole mass spectrometer. Approximately 15 mg of sample was loaded into an alumina crucible. Argon was flowed through the sample chamber at 50 SCCM while the temperature was ramped from room temperature to 1000 °C at a rate of 20 °C per minute while TG and MS signals were recorded.

2.2.7. CO-Temperature programmed reduction (CO-TPR)

CO-TPR experiments were carried out by loading a 200 mg portion of each sample into a 7 mm ID quartz tube between quartz wool plugs. The sample tube was housed inside a programmable electrical tube furnace. Each sample was pretreated by flowing Ar (50 SCCM) and holding the furnace at 200 °C for one hour, then allowing to cool to room temperature. A 5% mixture of carbon monoxide in argon was flowed at 50 SCCM and the furnace was ramped from

room temperature to 800 °C at a rate of 10 °C/min. The reactor outlet gases were analyzed using an MKS e-Vision⁺ quadrupole mass spectrometer (residual gas analyzer).

2.3. Catalytic evaluation for total CO oxidation

The catalytic oxidation of CO to CO₂ over different manganese oxide materials was conducted in a fixed-bed flow-type quartz tube reactor. A 100 mg sample of each catalyst was loaded in the reactor and pretreated for 1 h by passing Ar gas (20 SCCM) through the samples heated at 120 °C to completely dry and remove adsorbed surface species. The reaction was started by flowing the gas mixture (1% CO, 1% O₂, and 98% N₂ (internal standard)) through the reactor at a fixed flow rate of 20 SCCM at varying reaction temperatures (0–200 °C). Online analyses of effluent gas were taken at each temperature after a stabilization time of 20 min on-stream using an SRI model 8610C gas chromatograph equipped with a thermal conductivity detector (TCD). Helium was used as the carrier gas for all analyses. The peak areas of CO, O₂, N₂, and CO₂ were proportional to concentration. The initial concentration of CO was corrected using Eq. (1). The corrected peak area of CO was used to calculate the % conversion as shown in Eq. (2).

$$\frac{(\text{PeakareaCO})_{\text{initial}}}{(\text{PeakareaN}_2)_{\text{blank}}} = \frac{((\text{PeakareaCO})_{\text{blank}} \times (\text{PeakareaN}_2)_{\text{sample}})}{(\text{PeakareaN}_2)_{\text{blank}}} \quad (1)$$

$$\% \text{Conversion} = \frac{((\text{PeakareaCO})_{\text{initial}} - (\text{PeakareaCO})_{\text{sample}})}{(\text{PeakareaCO})_{\text{initial}}} \times 100\% \quad (2)$$

Activities versus time curves were also obtained for undoped K-OMS-2 materials and Ni and Rh doped K-OMS-2 materials in order to study their deactivation properties by passing the gas mixture (1% CO, 1% O₂, and 98% N₂ (internal standard)) through the sample at their corresponding T₅₀ (temperature at 50% conversion) over a period of 150 min. Effects of the flow rate were studied by using different flow rates (10, 20, 40 SCCM) over the K-OMS-2(REF) catalyst. A diagram of the CO oxidation reactor is shown below in Fig. S1.

3. Results

3.1. Catalytic performance toward CO oxidation

3.1.1. CO oxidation activity of different manganese oxide materials

The catalytic performance of the manganese oxides, expressed as the average % CO conversion to CO₂ as a function of temperature, is shown in Fig. 1a. All manganese oxide materials showed 100% CO conversion when the temperature was increased up to 200 °C. K-OMS-2(SF) showed a CO conversion of 7% even at 0 °C. K-OMS-2(SF) showed initial CO oxidation activity up to 75 °C, however their kinetics changed above that and reached 100% conversion at around 100 °C. K-OMS-2(REF) and Na-OMS-2 showed comparable activities towards CO oxidation where they reached 100% conversion between 125 and 150 °C. Cs-OMS-2 showed a slightly lower CO oxidation activity where CO oxidation began at 50 °C and reached 100% CO conversion at 200 °C. Differences between Cs-OMS-2 compared to K-OMS-2 and Na-OMS-2 were also observed in their structural characterization. As shown in Fig. S2a the Raman scattering spectra of K-OMS-2, Na-OMS-2, and Cs-OMS-2 featured four main contributions at 183, 387, 580, and 636 cm⁻¹ and to weak adsorption bands. However, the intensity ratios between bands at 580 and

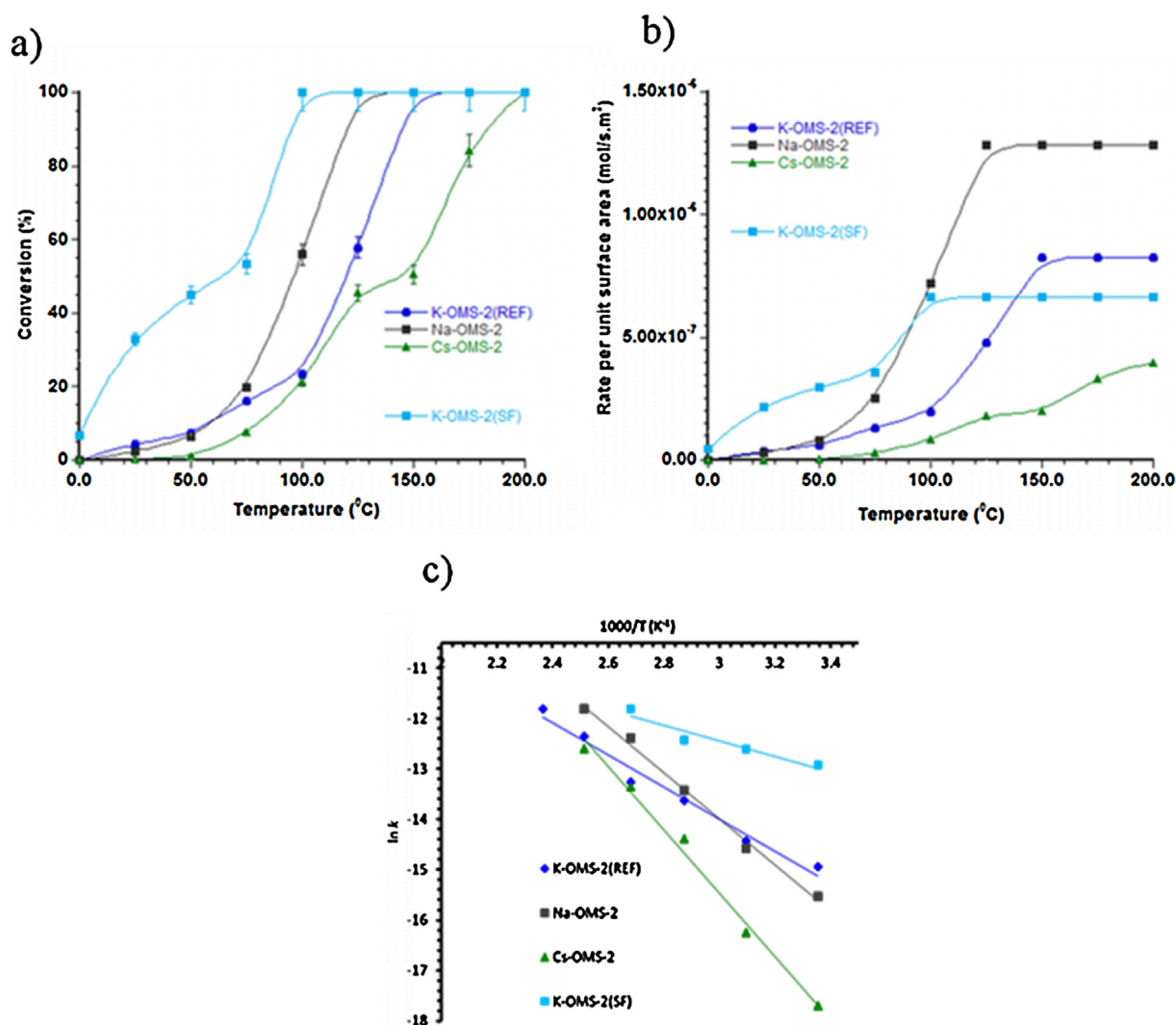


Fig. 1. a) % CO conversion and b) CO oxidation rates per unit surface area as a function of temperature and c) Arrhenius plots for CO oxidation over manganese oxide materials.

636 cm⁻¹ (I_{580}/I_{636}) for K-OMS-2 (1.19) and Na-OMS-2 (1.13) were greater than 1 while that of Cs-OMS-2 (0.86) was less than 1.

For a better understanding of the dependence of CO oxidation activity on the number of active sites, the CO oxidation rate per unit surface area has been plotted as a function of temperature (Fig. 1b). K-OMS-2(SF) showed an initial rate per unit surface area at 0 °C, however the reaction rate only slightly increased upon an increase of temperature. Both Na-OMS-2 and K-OMS-2(REF) showed similar shapes in their rate per unit surface area curves, although Na-OMS-2 obtained its maximum rate per unit surface area at a lower temperature as compared to K-OMS-2(REF) (125 vs. 150 °C). The same trends in % CO conversion profiles were observed for Cs-OMS-2, where the same maximum rate per unit surface area was reached. Activation energy of CO oxidation as a function of cobalt metal loading in K-OMS-2 was studied. The results show a decrease in activation energy for 1% Co-OMS-2 and 5% Co-OMS-2 materials when compared to K-OMS-2. However, when the metal loading increased, an increase in the activation energy is observed. The 10% Co-OMS-2 material showed a drastic increase in the activation energy compared to 1% Co-OMS-2, 5% Co-OMS-2 and K-OMS-2 materials.

Arrhenius plots for CO oxidation over manganese oxide materials are shown in Fig. 1c. The linear ranges between room temperature and 125 °C were selected in order to calculate the

apparent activation energies (E_a) since the objective of this study is to benchmark manganese oxide materials for catalytic low temperature aerobic oxidations. Table S1 shows the apparent E_a values of manganese oxide materials where the highest (15.9 kcal/mol) is for OMS-7. In addition, Cs-OMS-2 (12.4 kcal/mol), and Na-OMS-2 (9.10 kcal/mol) also showed higher activation energies for CO oxidation. Therefore K-OMS-2(SF) and K-OMS-2(REF), of which the activation energies were 3.0 and 6.3 kcal/mol respectively, were considered as possible candidates for low temperature selective oxidation. Further studies were then carried out in order to observe the effects of doping with foreign metal ions on CO oxidation activity.

3.1.2. CO oxidation activity of different metal ion doped K-OMS-2 materials

Fig. 2a shows the average % CO conversion to CO₂ as a function of temperature of the metal ion doped K-OMS-2 materials. The % CO conversions of K-OMS-2(REF) and K-OMS-2(SF) are also plotted as a control. Out of all the doped materials, Rh-K-OMS-2 showed a significant initial activity towards CO oxidation. However at around 80 °C, Rh-K-OMS-2 started showing a similar activity to Ni-K-OMS-2 reaching 100% conversion at around 125 °C. On the other hand, the CO oxidation activities of In-K-OMS-2, Fe-K-OMS-2, and Re-K-OMS-2 were the lowest and only Fe-K-OMS-2 was able to convert

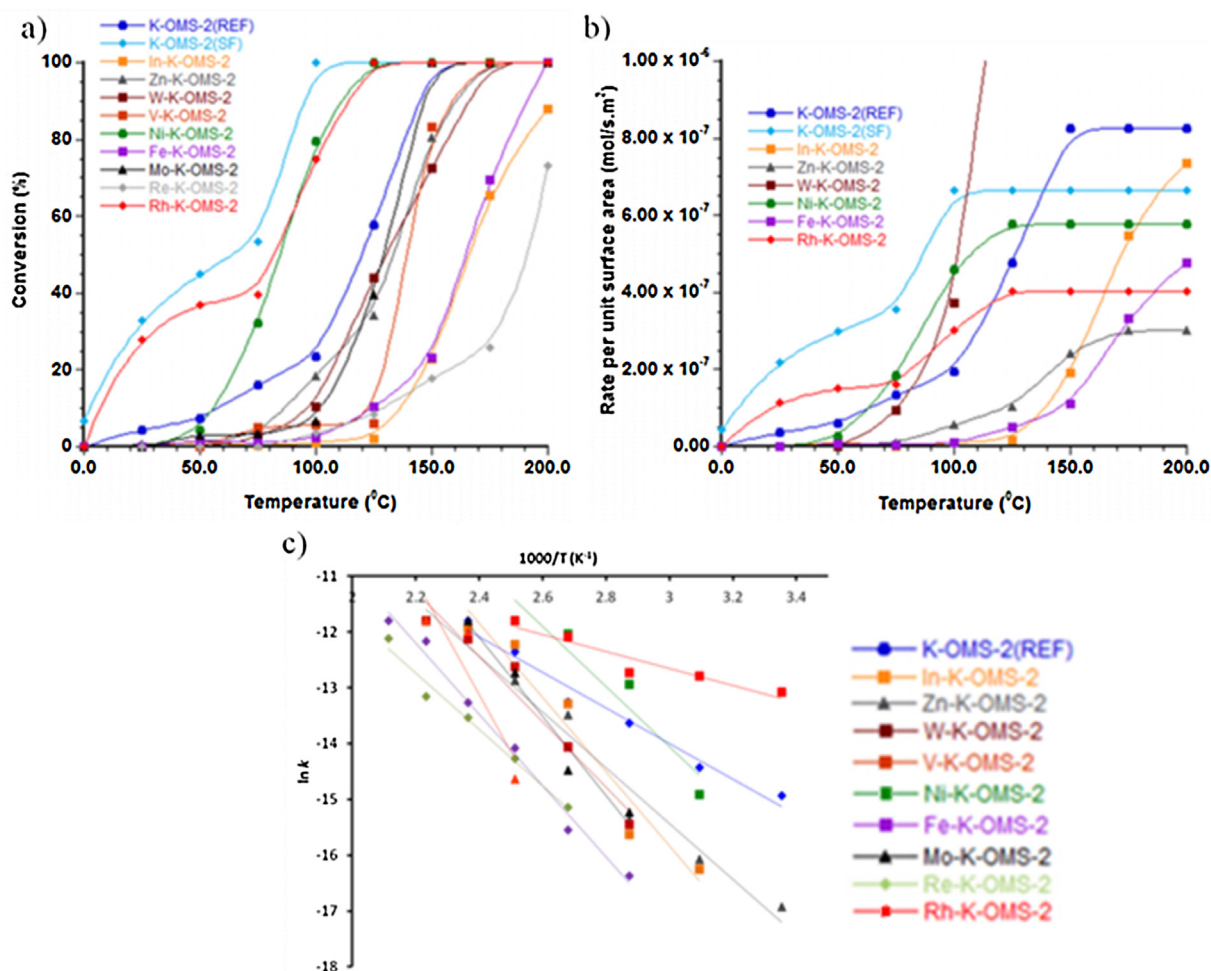


Fig. 2. a) % CO conversions b) CO oxidation rates per unit surface area as a function of temperature and c) Arrhenius plots for CO oxidation over metal ion doped K-OMS-2 materials.

100% CO to CO₂ at 200 °C. Zn-K-OMS-2, W-K-OMS-2, V-K-OMS-2, and Mo-K-OMS-2 showed intermediate activity towards CO oxidation reaching 100% CO conversion between 150 and 175 °C. Fig. 2b shows the CO conversion rate per unit surface area of the metal ion doped K-OMS-2 materials as a function of temperature. Although there is no activity below 50 °C, the rate per unit surface area of W-K-OMS-2 was increased drastically with higher reaction temperatures. However, this might be observed due to the relatively low surface area of W-K-OMS-2 (21 m²/g). A similar observation was made for Ni-K-OMS-2, where its rate per unit surface area is lower than that of Rh-K-OMS-2 in the low temperature region (<75 °C) and increases rapidly above 75 °C. The observed trend in CO oxidation activity of the doped materials can be related to their structural characteristics. Rh and Ni-K-OMS-2 materials showed the highest CO oxidation activities, V-K-OMS-2 showed an intermediate activity and In-K-OMS-2 showed the lowest activity (Fig. 2a). Fig. S2 shows the Raman spectra of Rh-K-OMS-2, Ni-K-OMS-2, V-K-OMS-2, and In-K-OMS-2. The observed Raman spectra show that I₅₈₀/I₆₃₆ ratios and intensities of all the peaks increase going from Rh-K-OMS-2 to In-K-OMS-2 (Fig. S2).

Arrhenius plots for CO oxidation for metal ion doped K-OMS-2 materials are shown in Fig. 2c. The linear range between room temperature and 200 °C was chosen to calculate the E_a. Among the metal ion doped K-OMS-2 materials, Rh-K-OMS-2 has the lowest E_a for CO conversion to CO₂ (3.00 kcal/mol), while V-K-OMS-2 has the highest E_a (20.34 kcal/mol) (Table S2).

3.1.3. CO oxidation activity of Ni-K-OMS-2 and Rh-K-OMS-2 materials

In the analysis of % CO conversion as a function of temperature of the M-K-OMS-2 materials, Ni-K-OMS-2 and Rh-K-OMS-2 showed superior activity over the other metal ion doped materials. The observed trend in CO oxidation activity of the doped materials can be related to their structural characteristics.

As depicted in Fig. 3a, Ni-K-OMS-2 and Rh-K-OMS-2 showed a wide range of CO conversion activity based on the synthesis method used. These experiments were mainly focused on the comparison of the activities between materials synthesized by reflux and solvent free methods; however, Ni and Rh-K-OMS-2 materials synthesized by microwave assisted hydrothermal method (MWHY) were also analyzed in order to further understand the significance of the synthesis method. In both Ni and Rh-K-OMS-2 materials the CO conversion decreased in the order of solvent free (SF) synthesis, reflux (REF) synthesis, and microwave assisted hydrothermal (MWHY) synthesis. Although Rh-K-OMS-2 showed a higher initial activity (<10% conversion) compared to Ni-K-OMS-2, at around 75 °C, the CO conversion activity of Ni-K-OMS-2 synthesized by SF and REF synthesis methods significantly increased. In contrast to that, Ni-K-OMS-2(MWHY) always showed a higher CO oxidation activity compared to Rh-K-OMS-2(MWHY).

The E_a values obtained from analyzing the Arrhenius plots (Fig. 3c), are listed in Table S4. The E_a values range from 3.0–22.1 kcal/mol where Rh-K-OMS-2(SF) and Ni-K-OMS-2(REF) were the lowest and Rh-K-OMS-2(MWHY) and Ni-K-OMS-

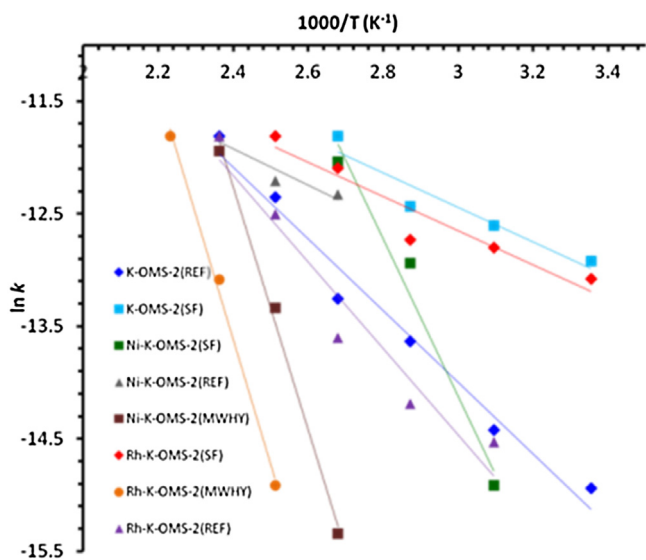


Fig. 3. Arrhenius plots for CO oxidation over materials synthesized by reflux (REF), solvent free (SF), and microwave assisted hydrothermal methods (MWHY).

2(MWHY) were the highest. Rh-K-OMS-2(REF) (7.7 kcal/mol) and Ni-K-OMS-2(SF) (13.9 kcal/mol) had intermediate E_a values.

3.1.4. CO% conversions as a function of reaction time over Ni-K-OMS-2 and Rh-K-OMS-2 materials the effect of feed gas flow rate on CO oxidation

As shown in Fig. 4a, the stability of the catalysts towards CO oxidation as a function of time was determined by conducting the CO oxidation experiments at their respective T_{50} (T_{50} = temperature at which 50% conversion is observed) over a period of 150 min. Interestingly, both K-OMS-2(REF) and Rh-K-OMS-2(REF) did not show any change in activity and remained at 50% conversion. However, the activity of Ni-K-OMS-2(REF) slightly decreased (by 2% CO conversion) up to 60 min and stabilized at about 48% CO conversion. All the catalysts prepared from the solvent free method showed a lower stability compared to the catalysts prepared from the reflux method. The stability of Ni-K-OMS-2(SF) was greater compared to the undoped counterpart (46% vs. 42%) however, that of Rh-K-OMS-2(SF) was much lower. Ni-K-OMS-2(SF) and Rh-K-OMS-2(SF) reached stable CO% conversions at 46% and 34% respectively. The undoped K-OMS-2(SF) material did not stabilize over the period of the experiment. On the other hand, Ni-K-OMS-2(SF) and Rh-K-OMS-2(SF) materials stabilized after 60 min and 90 min respectively. Since the present study is based on heterogeneous catalysis, the effect of gas flow rate on the CO oxidation activity was determined by using K-OMS-2(REF) as a reference (Fig. 4b). The highest activity was obtained when the flow rate was 20 SCCM while the least activity was obtained by 100 SCCM. In addition, the CO oxidation profiles when the flow rates were 20 and 40 SCCM, contained a linear portion indicating the absence of mass transfer limitations in the particular temperature range while no linear portion was observed when the flow rate was 10 SCCM. The T_{50} values at 10, 20, 40, 60 and 100 SCCM are around 145, 120, 155, 165, and 175 °C, respectively.

3.2. Characterization of Rh-K-OMS-2 and Ni-K-OMS-2 materials

3.2.1. Powder X-ray diffraction (XRD)

The XRD patterns of Rh-K-OMS-2 and Ni-K-OMS-2 along with the undoped K-OMS-2 materials are shown in Fig. S3. The materials consisted of all the typical peaks similar to the tetragonal structure of cryptomelane type manganese oxide indicating that there is not

any phase segregation. Interestingly, a clear correlation between the XRD peak intensity and the catalyst stability upon CO oxidation at T_{50} was observed (Fig. 4). Both K-OMS-2(REF) and Rh-K-OMS-2(REF) materials showed the highest intensities and they showed the highest stabilities. On the other hand, Ni-K-OMS-2(REF) consisted of less intense broader peaks and showed a lower stability compared to undoped K-OMS-2(REF). K-OMS-2(SF) also showed broader, less intense peaks. However, the peaks of Ni-K-OMS-2(SF) were slightly more intense and those of Rh-K-OMS-2(SF) were slightly less intense compared to undoped material. This is well supported by their stability tests where Ni-K-OMS-2(SF) was more stable and Rh-K-OMS-2(SF) was less stable compared to K-OMS-2(SF).

3.2.2. N_2 adsorption-desorption studies

Brunauer, Emmett and Teller (BET) Surface areas, Barrett-Joyner-Halenda (BJH) pore volumes, and BJH pore radii of Ni-K-OMS-2 and Rh-K-OMS-2 materials synthesized by reflux (REF), solvent free (SF), and microwave assisted hydrothermal methods (MWHY) from nitrogen sorption analysis are listed in Table S5. More rigorous calculations on pore sizes can be done by the methods suggested by Thommes et al. [22] The surface areas of Rh-K-OMS-2(REF), Ni-K-OMS-2(REF), and Rh-K-OMS-2(SF) are 201, 199, and 184 m²/g, respectively, and are the highest values of the series. On the other hand, Rh-K-OMS-2(MWHY) had the lowest surface area (84 m²/g) while Ni-K-OMS-2(MWHY) (104 m²/g) and Ni-K-OMS-2(SF) (129 m²/g) had intermediate values. Considering the pore volumes, Ni-K-OMS-2(REF) consisted of the highest (0.59 cc/g) while Rh-K-OMS-2(MWHY), Rh-K-OMS-2(REF), and Ni-K-OMS-2(SF) also had high pore volumes of 0.42, 0.40, and 0.39 cc/g, respectively. On the other hand, Ni-K-OMS-2(MWHY) and Rh-K-OMS-2(SF) had low pore volumes of 0.13, and 0.21 cc/g, respectively. All of the materials contain mesopores in the range of 3–12 nm.

3.2.3. Field emission scanning electron microscopy (FESEM)

The morphologies of the Rh-K-OMS-2 and Ni-K-OMS-2 materials grown by SF, REF, and MWHY methods are shown in their FESEM images (Fig. 5) and can be used to compare morphological differences of K-OMS-2 materials produced by different synthetic methods. Both Rh-K-OMS-2(SF) and Ni-K-OMS-2(SF) appeared as nano-crystalline structures while Rh-K-OMS-2(REF) and Ni-K-OMS-2(REF) appeared as nano-needle structures. Rh-K-OMS-2(MWHY) and Ni-K-OMS-2(REF) were observed as nanorod structures. Interestingly, the particle sizes of both Rh-K-OMS-2(REF) and Ni-K-OMS-2(REF) are larger than their respective materials synthesized by the solvent free method, although their surface areas are larger compared to the latter materials.

3.2.4. Inductively coupled plasma optical emission spectrometry (ICP-OES)

ICP-OES data for M-K-OMS-2(REF) are given in Table S6. Ni weight percentages with respect to Mn in Ni-K-OMS-2(SF) and Ni-K-OMS-2(REF) were 2.00% and 0.62% while the Rh amounts with respect to Mn in Rh-K-OMS-2(SF) and Rh-K-OMS-2(REF) were 0.20% and 0.82%.

3.2.5. CO temperature-programmed reduction (CO-TPR) analysis

The redox properties of metal oxide catalysts could be investigated by using temperature programmed reduction analysis. Fig. 6a presents the CO-TPR profiles of the undoped and Rh and Ni doped K-OMS-2 materials synthesized by reflux and solvent free methods corresponding to the formation of CO₂. According to the literature, [2,23] three peaks are expected to be observed for K-OMS-2 materials. The first peak at around 230 °C is related to labile O, the second peak is observed at around 295 °C due to the reduction of KMnO₁₆

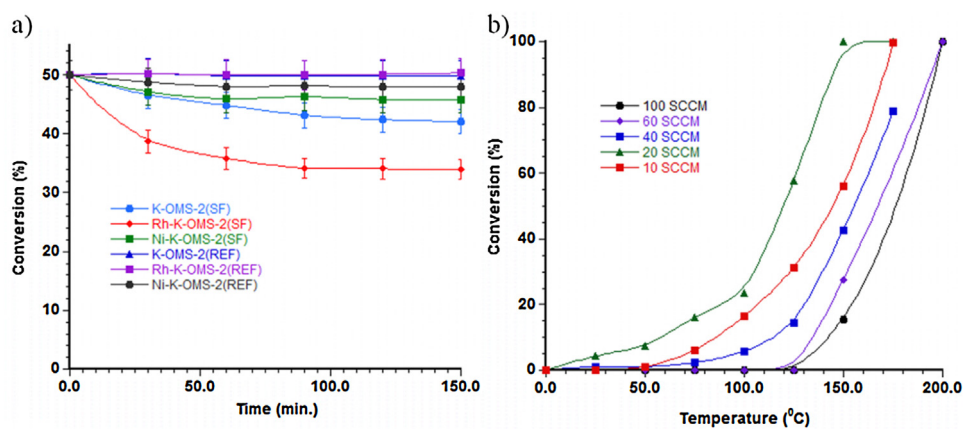


Fig. 4. a) CO% conversions at T_{50} as a function of reaction time over Ni-K-OMS-2 and Rh-K-OMS-2 materials b) CO conversions as a function of temperature over K-OMS-2(REF) at different flow rates.

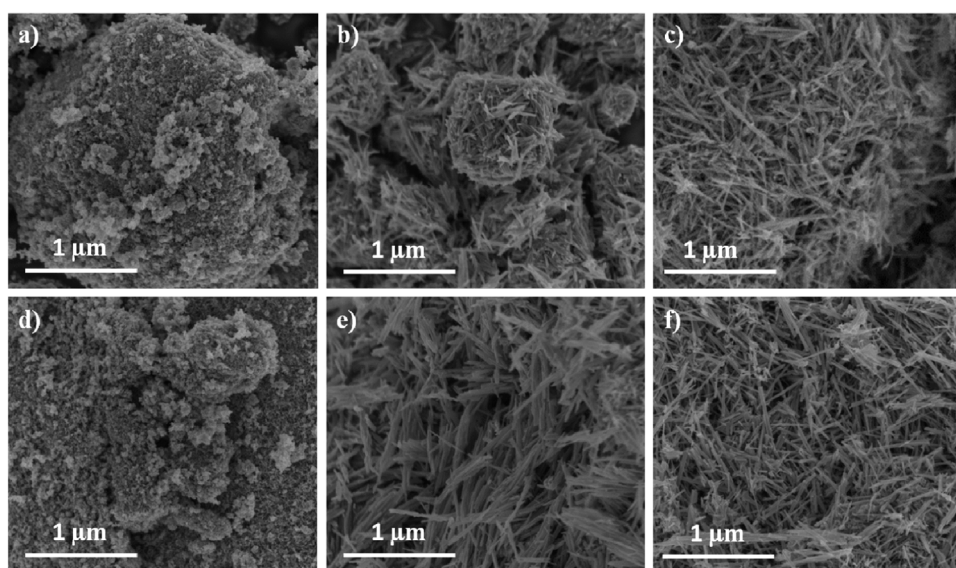


Fig. 5. FESEM images of a) Rh-K-OMS-2(SF) b) Rh-K-OMS-2(REF) c) Rh-K-OMS-2(MWHY) d) Ni-K-OMS-2(SF) e) Ni-K-OMS-2(REF) and f) Ni-K-OMS-2(MWHY) materials.

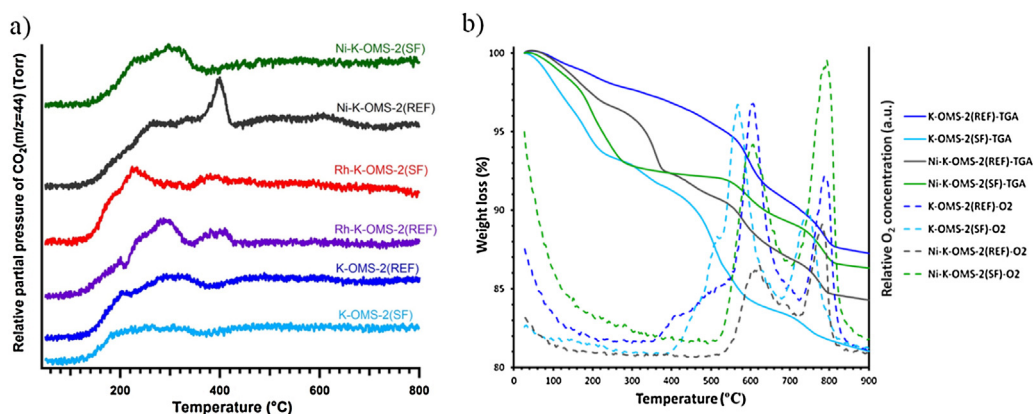


Fig. 6. a) CO-TPR profiles of undoped and Rh and Ni doped K-OMS-2 materials b) TGA and O_2 profiles of undoped K-OMS-2 and Ni-K-OMS-2 materials synthesized by reflux and solvent free methods.

to Mn_3O_4 , and the third peak observed at around 395°C is due to the reduction of Mn_3O_4 to MnO . In this study, although the undoped K-OMS-2 materials showed all 3 peaks in their CO-TPR profiles, the relative intensities were considerably low. However, in K-OMS-2(SF), the first two peaks were overlapped and shifted toward lower

temperature regimes compared to K-OMS-2(REF). This behavior is well observed in Rh-K-OMS-2(SF) where the intensity of the second peak was significantly high. Although the intensities of the first two peaks of Ni-K-OMS-2(SF) are comparable to those of Rh-K-OMS-2(SF), both of them were shifted towards the higher temperature

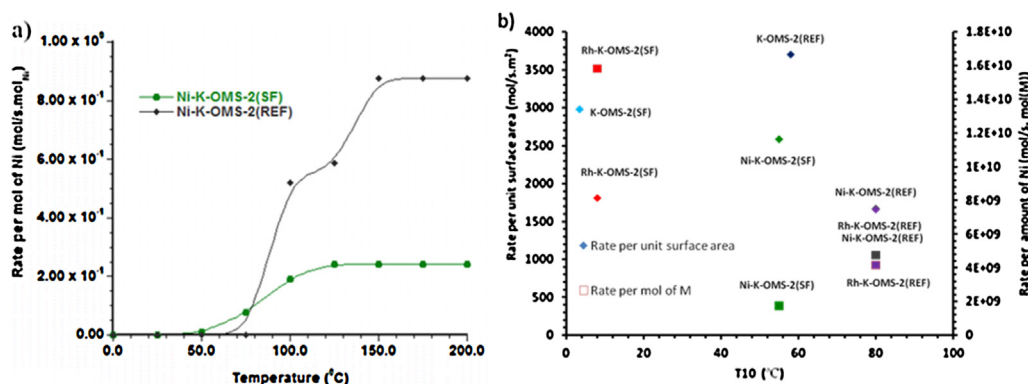


Fig. 7. a) CO conversion rate as a function of the amount of Ni present in Ni-K-OMS-2 materials b) CO conversion rates per unit surface area and per amount of Ni and Rh as a function of temperature at 10% conversion.

regime (184–228 °C and 228–298 °C). On the other hand, the first two peaks of both Rh and Ni-doped K-OMS-2(REF) materials were shifted towards the lower temperature regimes compared to their undoped counterpart although they were more intense in Rh-K-OMS-2(REF) than the Ni-doped material. However, the second peak of Ni-K-OMS-2(REF) was significantly shifted toward lower temperatures compared to the undoped material (307 to 268 °C). For all the catalysts the third peak remained at the same position. Interestingly, in Ni-K-OMS-2 the intensity of the third peak was markedly high.

3.2.6. Thermogravimetric analysis—mass spectrometry (TGA-MS)

Based on their CO oxidation activities and CO-TPR analysis Ni-K-OMS-2 materials showed unique characteristics. Ni based materials are more attractive due to their high abundance and low cost. Therefore, further analyses were conducted using Ni-K-OMS-2 materials in order to study their oxygen availability and dependence of CO oxidation activity on the amount of Ni in the structure. The thermogravimetric analysis-mass spectrometry (TGA-MS) analysis profiles of undoped and Ni-K-OMS-2 materials shown in Fig. 6b were similar in terms of shapes of the curves and the temperature zones where the major weight losses occurred. The first major loss which occurred between 30 and 250 °C was due to the desorption of water and O₂ from the surface which continued up to 580 °C due to the desorption of chemisorbed water. The second major weight loss occurred between 580 and 600 °C due to the evolution of structural oxygen near the surface without decomposing the material. The third major weight loss, occurred between 710 and 750 °C, and was attributed to the depletion of oxygen from the framework of the material where phase transformations from KMn₈O₁₆ to Mn₂O₃ and then to Mn₃O₄ take place. In the present study, Ni-K-OMS-2(SF) material is more stable and Ni-K-OMS-2(REF) is less stable with respect to their undoped materials upon heating which is in good agreement with the CO oxidation stability studies. K-OMS-2(SF) showed a significant weight loss from 30 to 250 °C compared to K-OMS-2(REF) (7% vs. 2%) and from 250 to 450 °C compared to both K-OMS-2(REF) and Ni-K-OMS-2(SF). However, the most noticeable weight loss was observed at 500–650 °C where K-OMS-2(SF), K-OMS-2(REF), and Ni-K-OMS-2(SF) showed weight losses of 7%, 4%, and 3.5% respectively. On the other hand, Ni-K-OMS-2(REF) showed only one significant weight loss which occurred from 250 to 300 °C (4%).

All the undoped and Ni doped materials produced two major oxygen desorption peaks. However, the undoped materials showed shoulder peaks beginning to appear at around 400 °C while both the doped materials started oxygen evolution at around 500 °C. Interestingly, the peak positions of both the oxygen peaks for K-OMS-2(SF) were shifted towards lower temperature regions

compared to the other 3 materials (568 vs. 609 °C and 743 vs. 791 °C). Moreover, the first oxygen peak of the undoped materials was more intense compared to the second peak whereas, the opposite was observed for the Ni doped material. In addition to that, both the oxygen peaks of Ni-K-OMS-2(SF) were more intense with respect to those of Ni-K-OMS-2(REF).

4. Discussion

Manganese oxides have been thoroughly studied as substitutes for noble metal catalysts in CO oxidation since they are inexpensive, readily available, and environmentally benign. In this study, CO oxidation activities have been examined by synthesizing pure and metal ion doped manganese oxide materials and extensive studies were carried out in order to identify possible catalyst materials for low temperature selective hydrocarbon oxidation. The disordered structure improves CO oxidation activity by increasing the available surface area.

OMS-2 materials are tunnel structured manganese oxides and they consist of 2 × 2 tunnels where eight surrounded edge shared and corner shared MnO₆ units which form a theoretical tunnel size of 4.6 × 4.6 Å. OMS-2 materials accommodate cations (Na⁺/K⁺/Cs⁺) and water inside the tunnel structure and provide high accessibility to reactant molecules not only on the surface but also in the bulk. The slightly lower activity shown by Cs-OMS-2 is attributed to the preferential growth direction as detected by Raman data. For OMS-2 materials, the band at 580 cm⁻¹ represents the Mn–O vibrations along the direction of the octahedral chain, while the band at 636 cm⁻¹ stands for Mn–O vibrations perpendicular to the direction of octahedral double chains. The more intense 636 cm⁻¹ band of Cs-OMS-2 suggests a preferential growth in the direction perpendicular to the direction of octahedral double chains over Na- and K-OMS-2. A detailed discussion of the assignment of these Raman signals and the significance of the intensity ratios is given in a previous publication [11]. Among the metal ion doped K-OMS-2 materials, Ni and Rh doped K-OMS-2 materials show superior activity due to their structural and electronic properties [24]. As shown in Fig. S2b, although the tunnel structure is favorable towards CO oxidation over the layered structure, the activity decreases as the tunnel length increases. One reason responsible for this might be the steric barrier inside the tunnel for reactants to adsorb and products to desorb. According to Figs. 3 a and 5, in both Ni and Rh-doped K-OMS-2 materials CO oxidation activities decrease while their crystallinity increases in the order of solvent free synthesis, reflux synthesis, and microwave assisted hydrothermal synthesis. Larger particle size, hence higher crystallinity, both reduce the surface area and therefore the CO oxidation activity decreases. According to ICP-OES data for metal doped M-K-OMS-

2(REF) materials incorporation of metal is highest for Fe-OMS-2 and lowest for W-OMS-2. Loading percentages range from 0.5% to 5.00%. There seems to be a decrease in CO oxidation activity of the materials as the loading percent increases. The results of ICP-OES elemental analyses for Co doped samples are given in Table S7. The Mn/K molar ratio has drastically increased compared to the initial ratio, confirming the removal of potassium ions occurred during the synthesis [23]. For all the materials, the Co/K ratio has increased compared to the initial ratio of the reactants. This indicates that a smaller amount of cobalt ions were removed as compared to the amount of potassium ions. When the amount of cobalt ion content increases up to 0.0471 mol/100 g in 10% Co-K-OMS-2, the manganese content decreases from 1.300 mol/100 g in undoped K-OMS-2 to 1.0240 mol/100 g in 10% Co-K-OMS-2. Regardless of the doping amount of Co, there is no significant change in the amount of potassium ions (mol/100 g) for both 1% and 5% doped Co-K-OMS-2. However, for 10% Co-K-OMS-2 there is a significant decrease in the amount of potassium ions, suggesting that at lower loading concentrations, manganese ions are substituted by cobalt ions, but at higher loadings, cobalt ions may begin to substitute potassium ions in the tunnels [23]. A slight line broadening is observed in Ni- and Rh-doped samples, which is attributed to the incorporation of these ions into the OMS-2 framework.

There is a similar trend in the activation energies as well. At lower loadings of Co (1% and 5%) the activation energies are very close and lower than that of K-OMS-2, but at higher Co loading (10%) the activation energy has drastically increased up to 80.82 kJ mol⁻¹. This indicates that, when the doped cobalt ions reside in the framework substituting for manganese ions, the activation energy of the reaction decreases whereas when the loaded cobalt ions substitute for potassium ions in the tunnels, the activation energy of the reaction increases.

Rh-K-OMS-2(SF) and Rh-K-OMS-2(REF) begin CO oxidation at 0 °C and room temperature respectively while the kinetics change at around 75 °C. However, Ni-doped materials do not show this kind of behavior and Ni-K-OMS-2(SF) and Ni-K-OMS-2(REF) begin CO oxidation at around 25 and 65 °C. The high initial activities of Rh-K-OMS-2 materials compared to Ni-K-OMS-2 materials might be due to higher adsorption of reactant species on Rh doped materials. At low O₂/CO ratios CO strongly adsorbs onto the surface of the Rh based catalyst whereas at high O₂/CO ratios Rh-based surfaces become saturated with oxygen atoms. Therefore, in this study, with O₂/CO 2:1, Rh-K-OMS-2 materials react rapidly at the beginning of reaction due to an abundance of the oxidant on the surface however the rate slows down as the temperature is increased due to less favorable CO adsorption [25]. A similar reaction profile is shown by K-OMS-2(SF) which might occur due to smaller particle size and high surface area. At around 75 °C and beyond, these materials follow the same reaction mechanism as the other K-OMS-2 materials where facile reversibility of oxygen re-adsorption takes place [23]. As Fig. 4a shows, all of the Ni and Rh-doped K-OMS-2 materials become stable after some time when the reaction takes place at a constant temperature. Although the undoped K-OMS-2(SF) material does not become stable after 150 min, doping the K-OMS-2(SF) with Ni and Rh enhances the efficiency of the Mars-van Krevelen mechanism. However, Ni-K-OMS-2(SF) reaches a higher final activity over Rh-K-OMS-2(SF), suggesting that the presence of Ni is more favorable for efficient oxygen reversibility. The materials synthesized by reflux methods do not show a significant difference, although the Ni-K-OMS-2(REF) shows slightly lower activity which will be discussed later. Based on the results observed in Fig. 4b, 20 SCCM is the optimum velocity (WHSV = 1.2 × 10³ mL h⁻¹ g⁻¹, where WHSV is the weight hourly space velocity). At higher WHSVs the activity decreases due to lower residence time and mass transfer limitations.

Considering the CO oxidation rate per unit surface area, both the Ni-K-OMS-2 materials show a higher activity compared to their respective Rh-K-OMS-2 materials (Fig. 3b). This might be due to the increased oxygen regeneration in the lattice structure when Ni is present. This idea is well supported by the CO-TPR data (Fig. 6a) where Ni-K-OMS-2 materials contain a lower amount of surface oxygen while evolving a larger amount of oxygen from the lattice structure. Ni-K-OMS-2(SF) gives off oxygen at a lower temperature and is easily reducible while Ni-K-OMS-2(REF) gets totally reduced to MnO giving off the most lattice oxygen at a higher temperature. TGA-MS results (Fig. 6b) are also consistent with the above hypothesis since Ni-K-OMS-2 materials do not exhibit the surface oxygen that their undoped counterparts evolved at 350–500 °C. In contrast to the undoped K-OMS-2 materials, the Ni-K-OMS-2 materials lose more oxygen from the structure as the temperature increases suggesting an abundance of weakly held surface oxygen in the lattice. The larger amount of oxygen in the Ni-K-OMS-2(SF) structure over the Ni-K-OMS-2(REF) structure is due to the difference in the amount of Ni present in the two materials. Ni-K-OMS-2(SF) contains a Ni amount that is four times than that of Ni-K-OMS-2. However, the CO oxidation activity with respect to the amount of Ni for Ni-K-OMS-2(REF) is more than four times the activity of Ni-K-OMS-2(SF). This might be due to the higher amount of Ni in the lattice structure in the Ni-K-OMS-2(REF) material as aqueous conditions, higher temperatures and reaction times (100 over 80 °C and 24 over 4 h) are used in the synthesis of Ni-K-OMS-2(REF) material. The idea is supported based on the CO-TPR data, where Ni-K-OMS-2(REF) gives an intense CO₂ peak due to structural reduction. According to the calculated activation energy values, the metal ion doped K-OMS-2 materials which are used for only selective oxidation in the previous studies, specifically show moderate values ranging from 9.1 to 14.0 kcal/mol (Na-OMS-2: 9.1 kcal/mol, Zn-K-OMS-2: 9.9 kcal/mol, W-K-OMS-2: 11.6 kcal/mol, Fe-K-OMS-2: 12.7 kcal/mol, Ni-K-OMS-2: 13.8 kcal/mol, and Mo-K-OMS-2: 14.0 kcal/mol).

5. Conclusions

CO conversion studies were successfully carried out using different manganese oxide materials and metal ion doped K-OMS-2 materials and the effects of their structural and electronic properties on the CO oxidation activity were discussed. As shown in Fig. 7b, Rh and Ni-doped K-OMS-2 materials synthesized by solvent free and reflux methods were identified as possible aerobic hydrocarbon oxidation catalysts based on their CO oxidation behavior. Other Ni and Rh-based catalysts have been widely used for low temperature methane oxidation [24]. Ni-K-OMS-2 materials were more attractive due to their low cost, abundance, and lower toxicity. Ni-K-OMS-2(SF) is a preferable catalyst for other selective oxidations due to a moderate activation energy value (13.88 kcal/mol) for CO oxidation. Based on the CO conversion profiles where oxidation starts at 25 and 65 °C and TGA-MS studies where no oxygen peaks are observed between 350 and 500 °C, the presence of small amounts of surface oxygen species inhibits the total oxidation of gaseous alkane substrates. Due to the presence of intense second and third peaks in Ni-K-OMS-2(SF) (at 298 °C) and Ni-K-OMS-2(REF) (at 395 °C) respectively in their CO-TPR studies, higher stability during the CO oxidation at a constant temperature, and more intense O₂ peaks observed in their TGA-MS studies, there is superior mobility and reversibility of the structural oxygen in Ni-K-OMS-2 materials. The present study demonstrates the factors affecting CO oxidation and how to predict a possible catalyst for low temperature selective oxidation and other selective oxidation reactions using CO oxidation behavior.

Acknowledgements

The scanning electron microscopy imaging was performed at the Biosciences Electron Microscopy Facility of the University of Connecticut, with financial support from NSF grant #1126100. We acknowledge ExxonMobil for support of this research. This work was partially supported by the US. Department of Energy, Office of Basic Energy Sciences, Division of Chemical Sciences, Geosciences, and Biological Sciences under grant DE-FG02-86ER13622.A000.

Appendix A. Supplementary data

Supplementary data associated with this article can be found, in the online version, at <http://dx.doi.org/10.1016/j.apcatb.2016.11.043>.

References

- [1] M. Özacar, A.S. Poyraz, H.C. Genuino, C. Kuo, Y. Meng, S.L. Suib, *Appl. Catal. A: Gen.* 462 (2013) 64.
- [2] H.C. Genuino, M.S. Seraji, Y. Meng, D. Valencia, S.L. Suib, *Appl. Catal. B: Environ.* 163 (2015) 361.
- [3] E.C. Njagi, C. Chen, H. Genuino, H. Galindo, H. Huang, S.L. Suib, *Appl. Catal. B: Environ.* 99 (2010) 103.
- [4] X. Ouyang, S.L. Scott, *J. Catal.* 273 (2010) 83.
- [5] J. Shen, R.E. Hayes, X. Wu, N. Semagina, *ACS Catal.* 5 (2015) 2916.
- [6] L. Wang, Q. Liu, X. Huang, Y. Liu, Y. Cao, K. Fan, *Appl. Catal. B: Environ.* 88 (2009) 204.
- [7] Y. Meng, W. Song, H. Huang, Z. Ren, S. Chen, S.L. Suib, *J. Am. Chem. Soc.* 136 (2014) 11452.
- [8] L.R. Pahalagedara, S. Dharmarathna, C.K. King'onde, M.N. Pahalagedara, Y. Meng, C. Kuo, S.L. Suib, *J. Phys. Chem. C* 118 (2014) 20363.
- [9] H.C. Genuino, S. Dharmarathna, E.C. Njagi, C.M. Mei, S.L. Suib, *J. Phys. Chem. C* 116 (2012) 12066.
- [10] B. Dutta, S. Biswas, V. Sharma, N.O. Savage, P.S. Alpay, S.L. Suib, *Angew. Chem.* 6 (2016) 2211.
- [11] H.C. Genuino, Y. Meng, D.T. Horvath, C. Kuo, M.S. Seraji, A.M. Morey, R.L. Joesten, S.L. Suib, *ChemCatChem* 5 (2013) 2306.
- [12] Y. Ding, X. Shen, S. Sithambaram, S. Gomez, R. Kumar, V.M.B. Crisostomo, S.L. Suib, M. Aindow, *Chem. Mater.* 17 (2005) 5382.
- [13] J. Liu, V. Makwana, J. Cai, S.L. Suib, M. Aindow, *J. Phys. Chem. B* 107 (2003) 9185.
- [14] C. Calvert, R. Joesten, K. Ngala, J. Villegas, A. Morey, X. Shen, S.L. Suib, *Chem. Mater.* 20 (2008) 6382.
- [15] R. Jothiramalingam, B. Viswanathan, T. Varadarajan, *Catal. Commun.* 6 (2005) 41.
- [16] E. Nicolas-Tolentino, Z. Tian, H. Zhou, G. Xia, S.L. Suib, *Chem. Mater.* 11 (1999) 1733.
- [17] H. Cao, S.L. Suib, *J. Am. Chem. Soc.* 116 (1994) 5334.
- [18] J. Jansson, *J. Catal.* 194 (2000) 55.
- [19] R. Xu, X. Wang, D. Wang, K. Zhou, Y. Li, J. Catal. 237 (2006) 426.
- [20] C.K. King'onde, N. Opembe, C. Chen, K. Ngala, H. Huang, A. Iyer, H.F. Garcés, S.L. Suib, *Adv. Funct. Mater.* 21 (2011) 312.
- [21] X. Chen, Y. Shen, S.L. Suib, C. O'Young, *Chem. Mater.* 14 (2002) 940.
- [22] M. Thommes, K. Kaneko, A.V. Neimark, J.P. Olivier, F. Rodriguez-Reinoso, J. Rouquerol, K.S.W. Sing, *Pure Appl. Chem.* 87 (2015) 1051.
- [23] H.C. Genuino, Y. Meng, D.T. Horvath, C. Kuo, M.S. Seraji, A.M. Morey, R.L. Joesten, S.L. Suib, *ChemCatChem* 5 (2013) 2306.
- [24] J.A. Velasco, C. Fernandez, L. Lopez, S. Cabrera, M. Boutonnet, S. Järäs, *Fuel* 153 (2015) 192.
- [25] M. Grass, Y. Zhang, D. Butcher, J. Park, Y. Li, H. Bluhm, K. Bratlie, T. Zhang, G. Somorjai, *Angew. Chem. Int. Ed.* 47 (2008) 8893.